# Freestanding $LiFe_{0.2}Mn_{0.8}PO_4$/rGO nanocomposites as high energy density fast charging cathodes for lithium-ion batteries

Florian Zoller[a, b], Daniel Böhm[a, c], Jan Luxa[d], Markus Döblinger[c], Zdeněk Sofer[d], Dmitry Semenenko[e], Thomas Bein[c], Dina Fattakhova-Rohlfing[a, b, e]*

[a]Forschungszentrum Jülich GmbH, Institute of Energy and Climate Research (IEK-1): Materials Synthesis and Processing, Wilhelm-Johnen-Straße, 52425 Jülich, Germany

[b]Faculty of Engineering and Center for Nanointegration Duisburg-Essen (CENIDE), Universität Duisburg-Essen, Lotharstraße 1, 47057 Duisburg, Germany

[c]Department of Chemistry and Center for NanoScience (CeNS), Ludwig-Maximilians-Universität München (LMU Munich), Butenandtstrasse 5-13 (E), 81377 Munich, Germany

[d]Department of Inorganic Chemistry, University of Chemistry and Technology Prague, Technická 5, 166 28 Prague 6, Czech Republic

[e]Laboratory of Physical and Chemical Processes in post Li-ion batteries, Moscow Institute of Physics and Technology, Institutsky lane 9, 141700 Dolgoprudny, Moscow District, Russia

*KEYWORDS: lithium ion batteries, cathode materials, lithium manganese phosphate, freestanding*

**ABSTRACT:** Freestanding electrodes for lithium ion batteries are considered as a promising option to increase the total gravimetric energy density of the cells due to a decreased weight of electrochemically inactive materials. We report a simple procedure for the fabrication of freestanding $LiFe_{0.2}Mn_{0.8}PO_4$ (LFMP)/rGO electrodes with a very high loading of active material of 83 wt%, high total loading of up to 8 mg $cm^{-2}$, high energy density, excellent cycling stability and at the same time very fast charging rate, with a total performance significantly exceeding the values reported in the literature. The keys to the improved electrode performance are optimization of LFMP nanoparticles via nanoscaling and doping; the use of graphene oxide (GO) with its high concentration of surface functional groups favoring the adhesion of high amounts of LFMP nanoparticles and freeze-casting of the GO-based nanocomposites to prevent the morphology collapse and provide a unique fluffy open microstructure of the freestanding electrodes. The rate and the cycling performance of the obtained freestanding electrodes are superior compared to their Al-foil coated equivalents, especially when calculated for the entire weight of the electrode, due to the extremely reduced content of inactive material (17 wt% of inactive material in case of the freestanding compared to 90 wt% for the Al-foil based electrode), resulting in 120 mAh $g^{-1}_{electrode}$ in contrast to 10 mAh $g^{-1}_{electrode}$ at 0.2C The better performance can also be attributed to the unique fluffy structure of the freestanding composite enabling an excellent contact between the LFMP nanoparticles and the electrolyte. The electrochemical performance of the freestanding LFMP/rGO electrodes is also superior compared to the values reported in literature for freestanding LFMP and LMP composites and can even keep up with those of LFP-based analogues. The freestanding LFMP/rGO reported in this work is additionally attractive due to its high gravimetric energy density (604 Wh $kg^{-1}_{LFMP}$ at 0.2C). The obtained results demonstrate the advantage of freestanding $LiFe_{0.2}Mn_{0.8}PO_4$/rGO electrodes and their great potential for applications in lithium ion batteries.

GRAPHICAL ABSTRACT

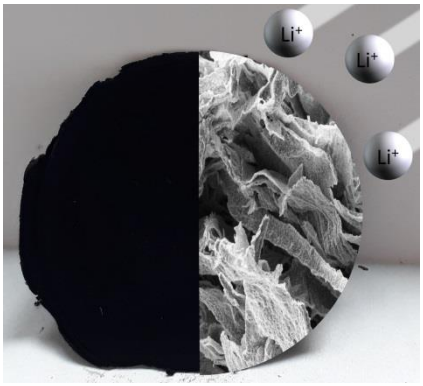


Freestanding $LiFe_{0.2}Mn_{0.8}PO_4$/rGO (LFMP/rGO) electrodes are prepared through the simple combination of ultrasonication, freeze-casting and pyrolysis. Rate and cycling performance of those freestanding electrodes are superior compared to the Al-foil coated equivalents as the content of electrochemically inactive material is drastically reduced demonstrating the great potential of freestanding electrodes for application in lithium ion batteries.

INTRODUCTION

Olivine-structured lithium transition-metal phosphates $LiMPO_4$ (M = Fe, Mn, Co, Ni) attract significant interest as cathode materials in Li-ion batteries (LIBs) due to their high theoretical specific capacities of around 170 mAh $g^{-1}$, good chemical and thermal stability, safety and low cost. Particularly, $LiFePO_4$ (LFP) has been already successfully commercialized.[1-3] Nevertheless, LFP has a rather low operating potential of 3.45 V vs. $Li/Li^+$ and a corresponding low energy density (568 Wh $kg^{-1}$), which hampers its application in high power and/or high energy devices.[1] Mn, Co or Ni based analogues gain increasing attention as promising alternatives having a similar theoretical specific capacity but higher energy densities of 701 Wh $kg^{-1}$, 802 Wh $kg^{-1}$ and 867 Wh $kg^{-1}$ for $LiMnPO_4$, $LiCoPO_4$ and $LiNiPO_4$, respectively.[4, 5] The redox potentials of $LiCoPO_4$ (4.8 V) and $LiNiPO_4$ (5.2 V) exceed the safe operational window of commonly used carbonate based electrolytes,[6] therefore $LiMnPO_4$ (LMP) with an operating potential of 4.1 V, being within the electrolyte stability window, is one of the most attractive olivine cathodes. LMP however suffers from major drawbacks like poor electrical conductivity and a low $Li^+$ diffusion rate, resulting in an inferior rate and cycling performance.[4, 6] Therefore, combinations of morphology optimization (such as nanoscaling and the formation of hybrids with carbonaceous conducting materials) and changing bulk properties via doping with other metals such as Fe (Fe-doped $LiMnPO_4$, LFMP) were established as efficient means to increase the electrochemical performance of LMP.[4]

In spite of the progress achieved, the theoretical capacity of $LiMPO_4$ of around 170 mAh $g^{-1}$ can still not be realized in practice, as electrodes typically consist of a mixture of the electrochemically active compound (e.g. LFP, LMP, LFMP, etc.) and inactive materials like a polymeric binder, carbonaceous conductor and aluminum foil as a current collector. For $LiFePO_4$, Susantyoko et al. calculated a maximum specific capacity of 121 mAh $g^{-1}_{electrode}$ when taking 29 wt% of inactive material into account (consisting of 22 wt% Al-foil and 7 wt% binder and conductor).[7] Similar values of inactive material and maximum achievable specific capacity can be expected for LMP and LFMP if the fraction of active material loading is at a scale typical for commercial devices. The weight fraction of electrochemically inactive materials is in fact even higher. Commonly reported electrodes consist of 80 wt% active material (in some cases electrochemically inactive components like graphene or carbon coatings are included as well) and 20 wt% carbon black and polymeric binder, coated altogether onto Al-foil with a thickness of 10 to 16 µm (density of Al: 2.7 g $cm^{-3}$, resulting areal density: 2.7 to 4.32 mg $cm^{-2}$). Active mass loadings are typically in the range of 1 to 6 mg $cm^{-2}$.[8-14] Taking these quantities into account, the amount of inactive material per electrode is increased to 43-82 wt%, implying that the maximum practical specific capacity is decreased to values as low as 31 mAh $g^{-1}_{electrode}$.

Fabrication of so-called “free- or selfstanding” electrodes is discussed to be an option to minimize the amount of inactive material since no aluminum foil is needed, which thereby increases the practical maximum specific capacity.[7, 15, 16] Freestanding cathodes typically consist of an active material (e.g. LFP), often embedded into a carbon-based matrix of

carbon nanotubes,[7, 17-19] graphene,[20-24] polymers,[20, 25] cellulose,[26, 27] carbon paper[15] or a mixture of two or more of the aforementioned compounds.

Freestanding electrodes can be fabricated by various techniques. For example, Xiao et al. introduced a two-step synthesis route. In a first step a reduced graphene oxide (rGO) poly(acrylic acid) aerogel was prepared, which was afterwards infiltrated with a LFP/carbon black/binder mixture.[20] Kretschmer et al. utilized a slightly different infiltration strategy, in which a paper towel was impregnated with LFP precursors and pyrolyzed to result in an LFP-carbon paper.[15] Li et al. demonstrated that graphene foam is also suitable for a similar preparation method.[21] Kanagaraj et al. and Susantyoko et al. used the so-called surface-engineered tape-casting, in which a carbon nanotube/LFP suspension is coated on a copper foil and the freestanding electrode is removed after the drying process.[7, 17, 19] Vacuum filtration of slurries consisting of LFP and diverse carbonaceous materials is another common strategy to prepare freestanding composites.[26-30] Finally, electrospinning is also a well-known method for the fabrication of freestanding electrodes.[16, 18, 31, 32] Notably, most of the available literature deals with freestanding LFP cathodes. The LMP and LFMP nanofiber composites reported by von Hagen et al. are the only examples of freestanding LMP-based cathodes reported so far.[16] However, in spite of significant efforts, the performance of freestanding electrodes is still not competitive to that of conventional electrodes. The main reason for that is still an insufficient amount of active material that can be incorporated into the freestanding electrode morphology, being typically around 70 wt%, and as a result relatively low energy densities per total weight of the electrodes.[7, 13, 31]

We report a simple procedure to fabricate freestanding $LiFe_{0.2}Mn_{0.8}PO_4$ (LFMP)/rGO electrodes with a very high loading of active material of 83 wt%, high total loading of up to 8 mg $cm^{-2}$, high energy density, excellent cycling stability and at the same time very fast charging rate, with a total performance significantly exceeding the values reported in the literature. The keys to the improved electrode performance are the use of GO with its high concentration of surface functional groups favoring the adhesion of high amounts of LFMP nanoparticles and, most importantly, the freeze-casting of the GO-based nanocomposites to prevent the morphology collapse and provide a unique fluffy open microstructure of the freestanding electrodes. To synthesize LFMP nanoparticles with an increased electrical conductivity and optimized size, a microwave-assisted synthesis in ethylene glycol was used. Freestanding electrodes were then prepared by simple mixing of LFMP nanoparticles and GO followed by an electrode casting in a novel freeze-casting approach. The resulting freestanding LFMP/rGO electrodes are composed of three-dimensionally interconnected rGO networks uniformly covered by a high amount of LFMP nanoparticles, hence enabling a full utilization of the active phase and a fast rate performance.

## RESULTS AND DISCUSSION

Scheme 1 depicts a simple novel fabrication process for the preparation of freestanding LFMP/C/rGO electrodes. In a first step LFMP nanoparticles obtained by a synthesis in ethylene glycol are mixed with GO and sucrose in water by ultrasonication (Step I). The following freeze-casting step (Step II) is comprised of pouring the homogenous ultrasonicated dispersion onto a liquid nitrogen pre-cooled aluminum block and subsequent freeze-drying of the obtained frozen composite. The resulting composite is finally pyrolyzed (Step III) leading to LFMP/C/rGO. Moreover, this fabrication process should also be feasible for preparation of different freestanding electrodes containing other materials than LFMP.

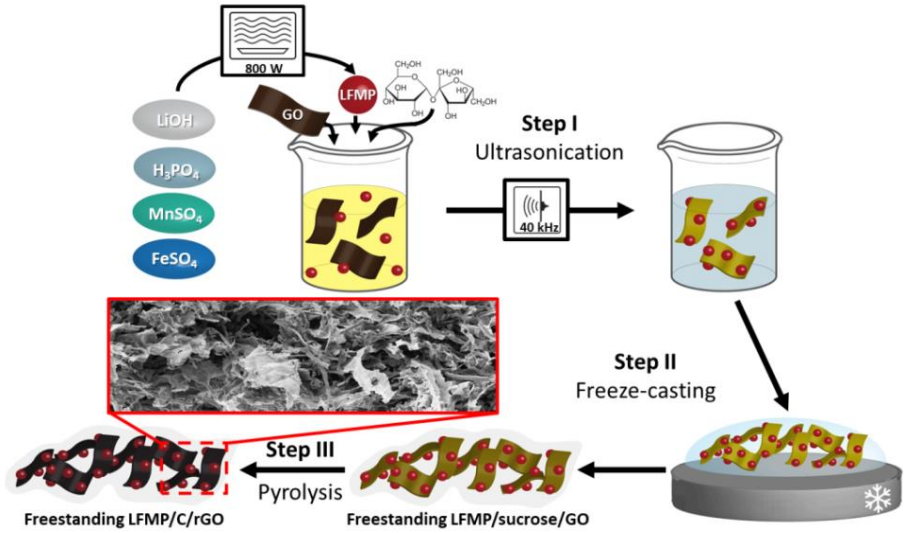


**Scheme 1.** Preparation of freestanding LFMP/C/rGO. Step I: Ultrasonication of microwave-assisted synthesized LFMP nanoparticles, GO and sucrose in water. Step II: Freeze-casting of the resulting homogenous dispersion. Step III pyrolysis of the obtained freestanding LFMP/sucrose/GO composite resulting in freestanding LFMP/C/rGO.

LFMP nanoparticles with 20 at% Fe doping, used in Step I (Scheme 1) were prepared in a microwave-assisted reaction in ethylene glycol (EG) using $MnSO_4$, $FeSO_4$, LiOH and $H_3PO_4$ as precursors, enabling a short reaction time of 25 min at 170 °C. Nanoscaling and doping with Fe atoms are the key prerequisites to improve the electrochemical performance of LMP materials due to their intrinsically poor electrical conductivity. 10 to 30 at% Fe (typically 20 at%) are reported as an optimum substitution range resulting in an improved conductivity together with an increased energy density.[33] X-ray diffraction patterns (XRD) of the obtained LFMP can be assigned to the olivine-structured LMP phase (JCPDS no. 74-0375) (Figure 1).

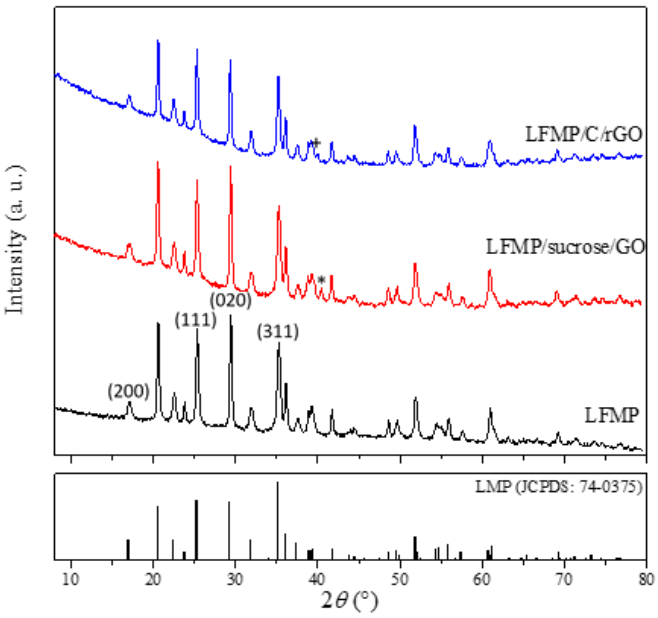


**Figure 1.** XRD patterns of LFMP, LFMP/sucrose/GO and LFMP/C/rGO. The bars at the bottom mark the position and the intensity of the diffraction lines of the olivine LMP structure (space group Pmnb, JCPDS no. 74-0375). The peaks marked with * and + are attributed to GO and rGO, respectively.

The positions of the diffraction peaks are slightly shifted to higher $2\theta$ angles as compared to the standard pattern of LMP, indicating the successful incorporation of Fe in the lattice and a partial substitution of Mn positions by Fe, thereby decreasing the lattice parameters.[34] Notably, the (020) diffraction peak in the obtained nanocrystalline product has the highest intensity instead of the (311) diffraction peak in the bulk reference pattern. Moreover, the ratio of $I(020)/I(200)$ is

calculated to be 6.2 and 6.8 for LFMP and LFMP/C/rGO, respectively, versus 2.6 for the LMP database reference entry. Such a high *I*(020)/*I*(200) ratio is reported to be advantageous for fast $Li^+$ ion transport rates.[8, 34, 35]

Scanning electron microscopy (SEM) and transmission electron microscopy (TEM) images reveal an elongated shape of the obtained nanoparticles with 10-18 nm width and 50-70 nm length (Figure S1 and S2). SEM/EDX element mapping as well as STEM/EDX mapping (high-angle annular dark-field (HAADF) STEM imaging mode) demonstrate a uniform distribution of Mn, Fe, P and O throughout the whole sample on the micro- and nanoscale (Figure S1c-f and S3). The elemental ratio of Fe/Mn is 0.20/0.80 (Table 1), which corresponds well to the targeted composition $LiFe_{0.2}Mn_{0.8}PO_4$. Similar results were obtained by inductively coupled plasma-optical emission spectrometry (ICP-OES) measurements featuring a Li/Fe/Mn ratio of 1.02/0.21/0.79 (Table 1).

**Table 1.** Atomic ratios of LFMP observed by ICP-OES and EDX (SEM/STEM).

| | Li | Fe | Mn | P | S |
|---|---|---|---|---|---|
| ICP | 1.02 | 0.21 | 0.79 | 0.88 | 0.15 |
| EDX (SEM) | - | 0.20 | 0.80 | 0.86 | 0.15 |
| EDX (STEM) | - | 0.20 | 0.80 | 0.86 | 0.15 |
| Theoretical (precursor input ratio) | 1 | 0.2 | 0.8 | 1 | |

ICP and EDX analyses indicate the presence of sulfur in addition to phosphorous with the sum of atomic fractions of S and P corresponding to 1, which possibly implies a partial occupation of P positions with S atoms. In the XPS spectrum of LFMP a small peak at 170 eV is detectable (Figure S4a), which is ascribed to S 2p and is typical for sulfates.[36, 37] Moreover, the uniform distribution of sulfur in the LFMP nanoparticles (Figure S3f) supports the assumption that S atoms are incorporated into the olivine lattice.

Other groups have also detected sulfur impurities in related olivine systems ($LiFePO_4$ and $LiCoPO_4$) synthesized via solvothermal reactions that could not be removed even by intensive washing.[38, 39] The nature of sulfur is not clear yet and may vary. Huang et al. assume that it originates from an insoluble impurity on the surface of LFP or that it is incorporated into the LFP lattice.[38] In contrast, Ludwig et al. concluded that an amorphous $Li_2SO_4$ phase is formed during the synthesis as a side product and is embedded to a certain degree into the $LiCoPO_4$ particles.[39] Okada et al. reported a partial substitution of oxygen sites in the LFP lattice by sulfur. However, in this case, thioacetamide was added as an additional sulfur source during the synthesis.[40]

In the next step of our synthesis procedure LFMP nanoparticles were mixed with sucrose and GO in water by intense ultrasonication and subsequently freeze-casted (Step I+II, Scheme 1 and Figure 2a). SEM and TEM images of the obtained LFMP/sucrose/GO composite reveal graphene oxide sheets that are well covered by LFMP particles (Figure S5). The deconvolution of the C1s peak in the XPS spectrum of GO (Figure S6a) reveals a high concentration of oxygen containing groups which are favorable for the adhesion of large amounts of LFMP. The most dominant (ca 40 at% according to the XPS data) are the C-O containing functional groups originating from carboxy, epoxy and alkoxy functionalities detectable in the FTIR spectrum (Figure S6b). Moreover, C=O and O-C=O functional groups are present in substantial concentrations of around 17 and 11 at.%, respectively. These results match with the elemental combustion analysis of GO demonstrating that CO consists of 54.1 wt% oxygen, 43.5 wt% carbon and 2.4 wt% hydrogen.

Additionally, Raman spectroscopy of GO reveals the typical D and G Raman bands at 1352 and 1594 $cm^{-1}$, respectively (Figure S6c).

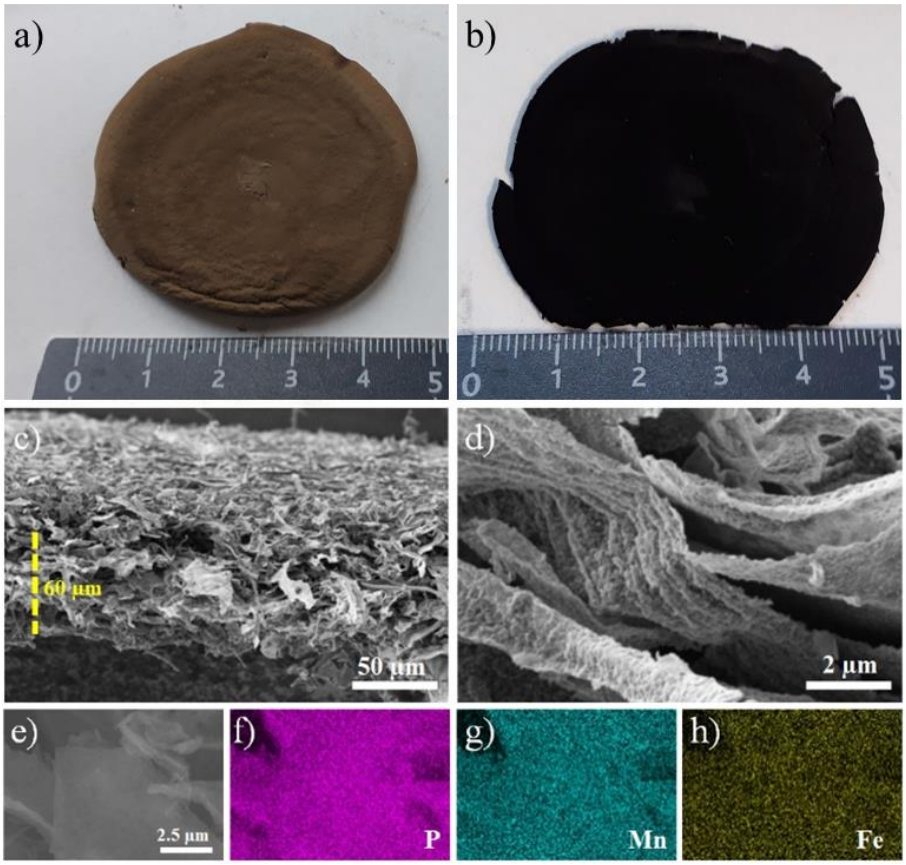


**Figure 2.** Photographs of the freestanding LFMP/sucrose/GO (a) and LFMP/C/rGO (b) samples. SEM images of cross section of freestanding LFMP/C/rGO nanocomposite (c-e). SEM micrograph of LFMP/C/rGO (e) and corresponding EDX element mappings illustrating the homogenous distribution of P, Mn and Fe (f-h).

To test whether a high concentration of oxygen containing groups is indeed beneficial for the adhesion of LFMP nanoparticles, multi-walled carbon nanotubes (MWCNTs) have been additionally added to the LFMP/sucrose/GO suspension before ultrasonication, as a reference experiment. The following steps remained unchanged. The SEM image of the pyrolyzed MWCNT containing composite (Figure S7) clearly demonstrates that the GO sheets are uniformly coated by LFMP particles whereas the MWCNTs are only sparsely covered, which is a distinct indication that the oxygen containing surface groups on GO promote the deposition of LFMP. Moreover, it should be noted that in our case the ultrasonication of preformed nanoparticle dispersions and GO provides a high loading of active material and allows for a homogeneous coverage of the GO sheets. In contrast, attempts to obtain LFMP/GO nanocomposites *in situ* during the nanoparticle synthesis in the presence of GO were not successful.

The diffraction pattern of the LFMP/sucrose/GO composite is very similar to that of pure LFMP. A small additional peak at around 40.4° 2$\theta$ is detectable, which is ascribed to GO. To carbonize the sucrose and to reduce GO to conducting rGO, the LFMP/sucrose/GO composites were pyrolyzed in nitrogen at 350 °C for 4 h and at 650 °C for 4 h. Thereby, the GO signal in the XRD pattern vanishes and additionally a small reflection at 40.0° 2$\theta$ (Figure 1) emerges that is assigned to rGO. The reduction of GO to rGO is furthermore supported by XPS analysis of the C1s peak of LFMP/sucrose/GO and LFMP/C/rGO (Figure S4b, c).

Importantly, the morphology of the LFMP/C/rGO freestanding composite is also preserved after pyrolysis (Step III, Scheme 1). The obtained black monoliths (Figure 2b) are approximately 4.5 cm in diameter and have typically a thickness of around 60 µm after slight compression. The weight fraction of LFMP in the LFMP/C/rGO nanocomposite is 83 wt% (Figure S8), detected by thermal gravimetric analysis (TGA), corresponding to LFMP loadings of around 3 mg/cm$^2$. Thicker layers with higher loading can be easily fabricated by stacking several layers of LFMP/sucrose/GO before pyrolysis. The size of the LFMP particles after pyrolysis remains very similar, with only a slight growth to reach 10-23 x 70-85 nm as observed in TEM and SEM images (Figures 2d and 3). The LFMP particles are still well dispersed on the rGO sheets after pyrolysis, as follows from the SEM and TEM images, together with element-mapping demonstrating homogenous element distribution (Figure 2f-h and S9). The SEM cross section images (Figure 2c, d) reveal that the rGO sheets form an interconnected three-dimensional network with open channels enabling good electrolyte permeation throughout the composite, which promotes $Li^+$ diffusion and hence can improve the electrochemical performance.[41] LFMP particles are covered by a thin uniform carbon layer with a thickness of around 2.5 nm (Figure 3b), which originates from the carbonization of sucrose. Such a coating layer can enhance the electron transport and $Li^+$ diffusion between the individual LFMP particles but can also protect the particles from manganese leaching into the electrolyte.[11, 42] Additionally, the carbon coating layer and the interconnected rGO sheets form a continuous conductive network enabling rapid electron transport, thereby overcoming one of the major disadvantages of LFMP, namely its low conductivity. The total increase of the electrical conductivity of composite electrodes was confirmed by 4-point conductivity analysis using the Van-der-Pauw method. The freestanding LFMP/C/rGO nanocomposite has an electrical conductivity of 0.94 S cm$^{-1}$, which is several magnitudes higher than the values reported for LMP and LFP.[6]

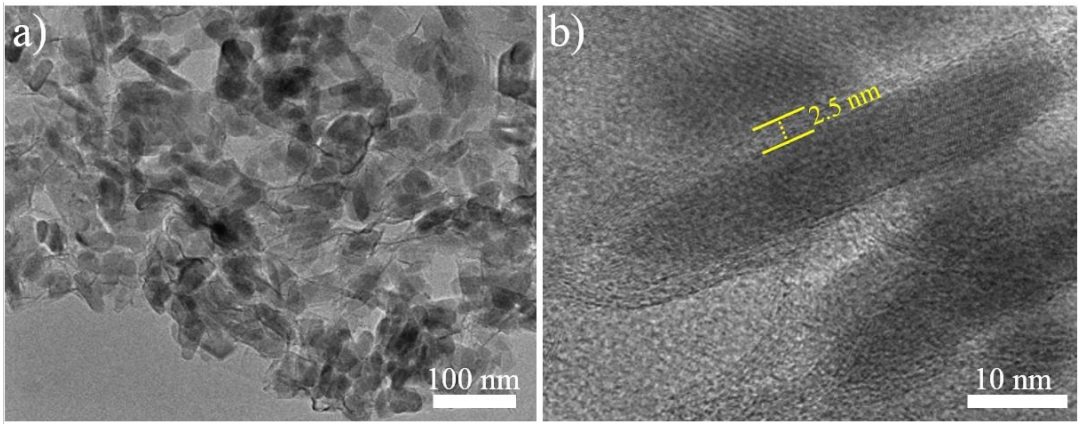


**Figure 3.** Low (a) and high (b) magnification HR-TEM images of LFMP/C/rGO.

Nitrogen physisorption measurements used to analyze the surface area and porosity of the LFMP/C/rGO composites (Figure S10) show type IV isotherms with an H2-type hysteresis loop typical for a mesoporous structure with disordered pores.[11] The BET surface area is 87 m$^2$ g$^{-1}$ and the corresponding total pore volume is 0.17 cm$^3$ g$^{-1}$ at $p/p_0 = 0.95$. In comparison, the pure LFMP particles feature a IV type isotherm with an H1 hysteresis loop, a slightly smaller BET surface area of 77 m$^2$ g$^{-1}$, and a total pore volume of 0.28 cm$^3$ g$^{-1}$ at $p/p_0 = 0.94$. The insets in Figure S10 show the pore size distribution of LFMP and LFMP/C/rGO. Upon incorporation of LFMP nanoparticles in LFMP/C/rGO composites, the pore size distribution gets narrower and shifts to lower values (ranging from 4 to 17 nm) as compared to the pure LFMP, probably caused by the formation of the carbon layer decreasing the pore volume. The porous morphology of the obtained composite is thereby beneficial for its use as an electrode layer since it can facilitate the infiltration with electrolyte resulting in an enhanced contact between electrolyte and primary LFMP particles.[9, 43]

The electrochemical performance of the freestanding LFMP/C/rGO nanocomposite was investigated using cyclic voltammetry (CV) and galvanostatic charge/discharge measurements. Importantly, the freestanding nanocomposites were directly used as a cathode; neither aluminum foil nor additional carbonaceous conductor or polymeric binder were used. Note that the specific capacity is based on the weight of the whole electrode if not mentioned otherwise, which includes LFMP, rGO and carbon in case of the freestanding composite or in addition the weight of Al-foil, carbon black and poly(vinylidene fluoride) (PVDF for conventionally fabricated composite reference electrodes) as well. This definition and determination of the specific capacity is different from the commonly used convention where the specific capacity is only reported per unit mass of active material. However, a specific capacity that comprises the total weight of the electrode will lead to a more accurate and realistic benchmarking of electrodes as the maximum achievable specific capacity is dependent on the amount of electrochemically inactive material.[20]

Figure 4a shows the first five CV curves of the freestanding LFMP/C/rGO nanocomposite between 2.0 and 4.5 V vs. $Li/Li^+$ at a scan rate of 0.1 mV $s^{-1}$ with two well-defined redox couples visible.

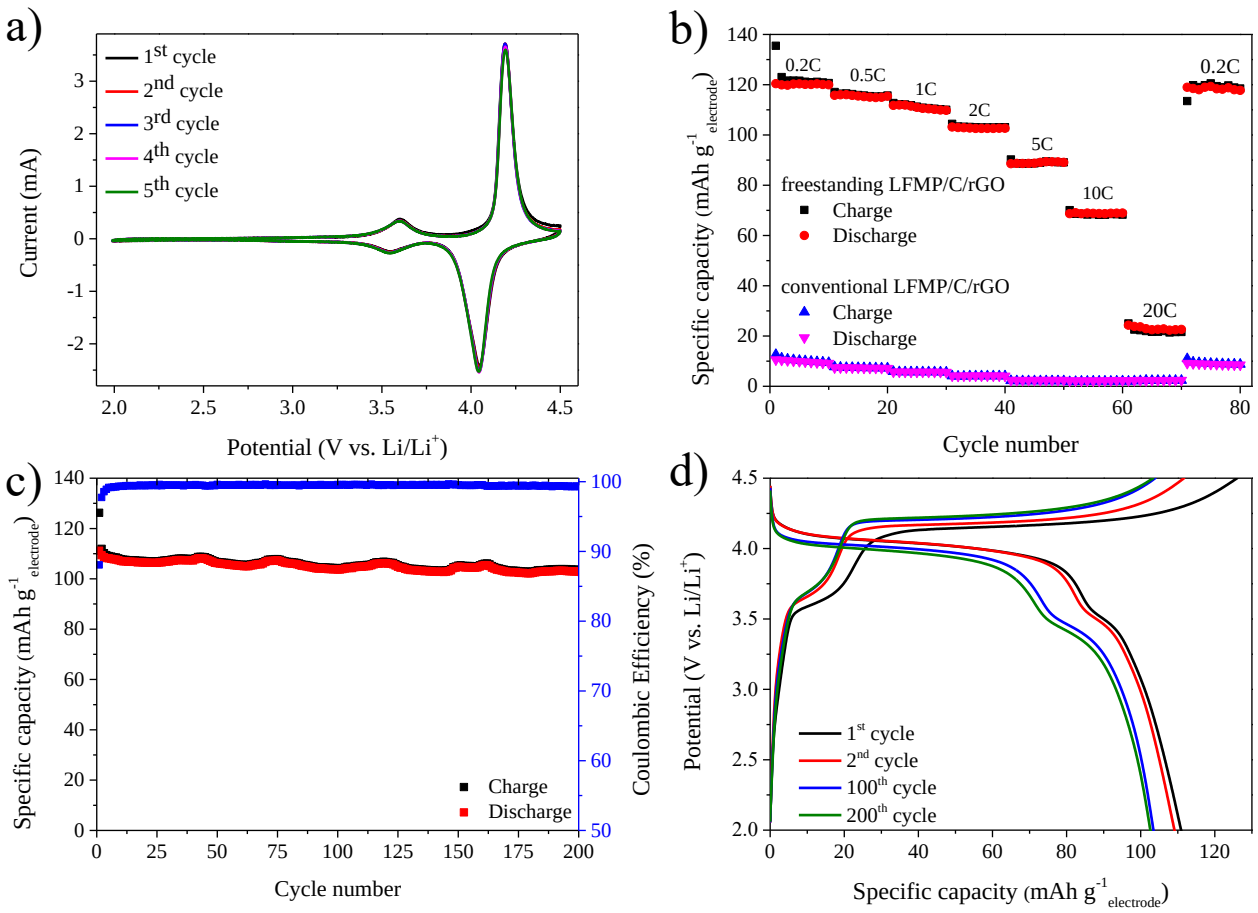


**Figure 4.** CV curves of freestanding LFMP/C/rGO electrode (a) recorded at a scan rate of 0.1 mV $s^{-1}$ in the range of 2.0-4.5 V vs. $Li/Li^+$. Rate performance (b) of freestanding and Al-foil based LFMP/C/rGO electrodes. Cycling stability and Coulombic efficiency (c) of freestanding LFMP/C/rGO electrodes over 200 cycles at 2C and the corresponding charge/discharge curves (d). Note that the galvanostatic measurements are all based on the total weight of the electrode. (LFMP loading of 3 and 0.6 mg $cm^{-2}$ for freestanding and Al-foil based LFMP/C/rGO electrodes, respectively).

The oxidation peaks at 3.60 and 4.19 V are thereby assigned to the oxidation of $Fe^{2+}$ to $Fe^{3+}$ and $Mn^{2+}$ to $Mn^{3+}$, respectively. The corresponding reduction reactions take place at potentials of 3.54 ($Fe^{3+}$ to $Fe^{2+}$) and 4.04 V ($Mn^{3+}$ to $Mn^{2+}$). The CV curves of the first five cycles practically overlap indicating high electrochemical stability without significant interface or bulk structural changes. The cycling stability was further evaluated by galvanostatic charge/discharge measurements at 2C (Figure 4c,d). The positions of the charge/discharge plateaus (Figure 4d) match well with the oxidation/reduction peak potentials recorded in the cyclic voltammograms. In the first cycle

charge/discharge capacities of 126 and 111 mAh $g^{-1}_{electrode}$ were achieved, respectively, which corresponds to a coulombic efficiency of 88%. Highly stable coulombic efficiencies of ≥ 99% are reached in subsequent cycles. After 200 cycles, 93% of the initial discharge capacity was retained, which corresponds to a discharge capacity of 103 mAh $g^{-1}_{electrode}$ (Figure 4), indicating an excellent cycling stability of the freestanding LFMP/C/rGO nanocomposite. It should be mentioned that small capacity fluctuations (ca 4-7 mAh/g) were observed for the rGO-based electrodes (Figure 4c). As similar capacity fluctuations were observed by us for other rGO-based composite electrodes (for example Sb:$SnO_2$/rGO electrodes described previously[44]) but not for pure electroactive materials (LFMP or Sb:$SnO_2$), it is reasonable to assume that the capacity fluctuations are related to the layered rGO morphology. As a possible reason the volume changes (breathing) during lithiation/delithiation or formation/dissolution of an SEI on the rGO-based electrode could be suggested, although further study is needed to evaluate the possible mechanism. Taking into account that the fluctuations are rather small and regular, any changes in the rGO-based electrodes should be however reversible or self-healing.

In order to test the rate performance of LFMP/C/rGO, different C-rates ranging from 0.2C to 20C were applied. Specific discharge capacities of 120, 115, 111, 103, 89, 69 and 22 mAh $g^{-1}_{electrode}$ are observed at 0.2C, 0.5C, 1C, 2C, 5C, 10C and 20C, respectively, recorded in the fifth cycle of each individual C-rate step. When the C-rate is returned to 0.2C, the initial discharge capacity is practically recovered (119 mAh $g^{-1}_{electrode}$). Moreover, the rate performance of the freestanding LFMP/C/rGO is far better than that of a conventionally prepared LMP/C/rGO electrode (LFMP/C/rGO mixed with carbon black, PVDF in 1-methyl-2-pyrrolidone (NMP) and coated onto Al-foil). The specific capacity of the Al-foil based LMP/C/rGO obtained at 0.2C is around 12 times smaller (Figure 4b), mainly attributed to the large amount of electrochemically inactive material of around 87 wt%.

To investigate the $Li^+$ ion intercalation kinetics in the freestanding and Al-foil based composite electrodes, CV curves at various scan rates ranging from 0.1 to 0.5 mV $s^{-1}$ shown in Figures 5a, c were recorded.

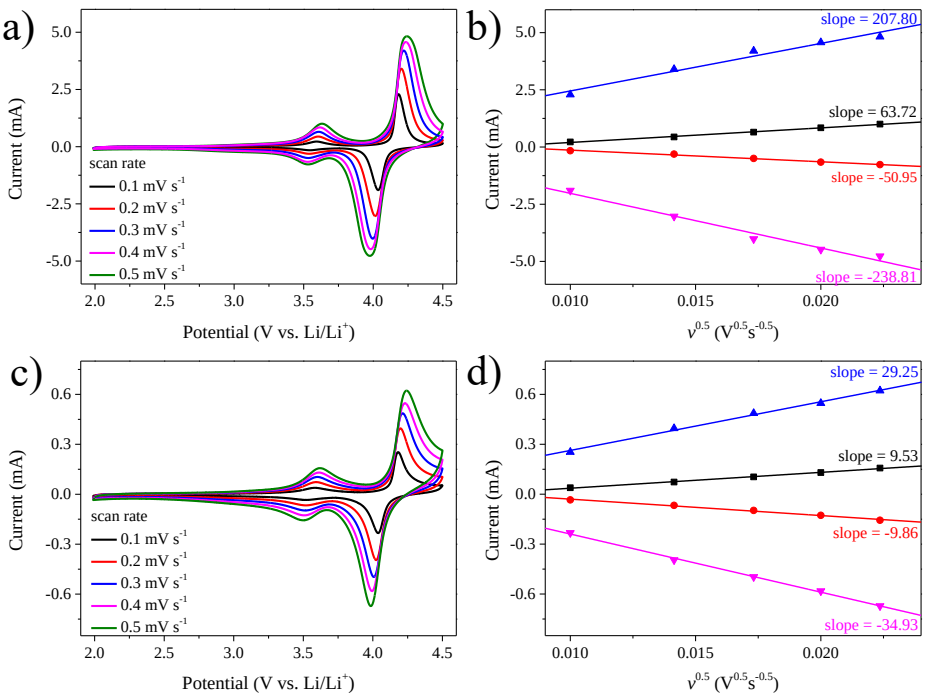


**Figure 5.** CV curves of freestanding (a) and Al-foil based (c) LFMP/C/rGO electrodes at different scan rates and resulting plots of the linear relationship between the peak current and the square root of the scan rate (b, d).

Upon an increase of the scan rate, the anodic peaks shift to higher potentials, whereas the cathodic counterparts shift to lower values. The peak currents ($I_P$) increase linearly with the square root of the scan rate ($v^{0.5}$) (Figure 5), indicating a

diffusion-controlled $Li^+$ de-/intercalation.[1, 8, 9, 15] Based on the above data, the $Li^+$ diffusion coefficients ($D$) can be calculated using the Randles-Sevcik equation:[1, 8, 9, 15]

$$I_p = 0.4463(nF)^{1.5}(RT)^{-0.5}C_{Li}A_eD^{0.5}v^{0.5} \qquad (1)$$

where $I_p$ is the peak current value, $n$ is the number of electrons in the charge transfer step ($n = 1$), $F$ is the Faraday constant ($F = 96485$ C mol$^{-1}$), $R$ is the gas constant ($R = 8.314$ J mol$^{-1}$ K$^{-1}$), $T$ is the absolute temperature ($T = 298.15$ K), $C_{Li}$ is the molar concentration of lithium ions in LFMP ($C_{Li} = 0.0222$ mol cm$^{-3}$), $A_e$ is the electrode area (here, the geometric area of the electrode is used for simplicity, $A_e = 2.54$ cm$^2$), $D$ is the $Li^+$ diffusion coefficient and $v$ is the scan rate.[9]

The calculated apparent $Li^+$ diffusion coefficients are listed in Table 2. We note that for the calculation of the $Li^+$ coefficients the geometric surface area of the electrodes instead of the area of the active nanocrystalline LFMP phase is used, the latter of which is otherwise difficult to determine. Therefore, the obtained values of $D$ do not provide the bulk diffusivity of the Li ions in the LFMP phase, but an apparent diffusion coefficient in the complete electrode structure.

The apparent $Li^+$ diffusion coefficients of the freestanding LFMP/C/rGO nanocomposite (Table 2) are around two orders of magnitude larger than those of the conventional Al-foil based electrodes. This finding shows that the freestanding LFMP/C/rGO nanocomposite enables improved $Li^+$ transport and diffusion, which could be a reason for the superior rate performance of the freestanding composite.

**Table 2.** Apparent $Li^+$ diffusion coefficients of freestanding and Al-foil based LFMP/C/rGO.

| State | Peaks | $Li^+$ diffusion coefficient $D$ [cm s$^{-1}$] | |
|---|---|---|---|
| | | Freestanding | Al-foil based |
| Charge | $A_{Fe}$ | 1.76 x 10$^{-11}$ | 3.94 x 10$^{-13}$ |
| | $A_{Mn}$ | 1.87 x 10$^{-10}$ | 3.71 x 10$^{-12}$ |
| Discharge | $C_{Fe}$ | 1.13 x 10$^{-11}$ | 4.22 x 10$^{-13}$ |
| | $C_{Mn}$ | 2.48 x 10$^{-10}$ | 5.30 x 10$^{-12}$ |

One of the possible reasons for the superior performance of freestanding electrodes can be their lower total resistance (higher conductivity) as compared to the same layers on an Al foil. Accordingly, in the Nyquist plots of both electrodes (Figure S11), the real part of the semicircle in the high frequency region corresponding to the charge transfer resistance ($R_{CT}$) is significantly smaller for the freestanding electrode as compared to the Al foil-based one (0.46 and 14.33 Ω, respectively).[30]

A comparison of the SEM images of the Al-foil based and the freestanding LFMP/C/rGO electrodes reveals significant differences between both morphologies. The freestanding electrode has a fluffy morphology as described above (Figure 2). In contrast, this structure is collapsed in case of the Al-foil based electrode, presumably caused by the slurry preparation process (Figure S12). The resulting denser morphology very likely hampers the infiltration of the electrolyte, diminishes the LFMP/electrolyte contact area and can be a reason for the lower $Li^+$ diffusion coefficient. Importantly, the freestanding LFMP/C/rGO electrodes retain their morphology and structural integrity even after the rate performance test. XRD patterns and SEM images of the cycled electrodes practically do not differ from the freshly prepared ones

(Figure 6). These results demonstrate the excellent structural stability of the freestanding LFMP/C/rGO electrode even at high rates of up to 20C.

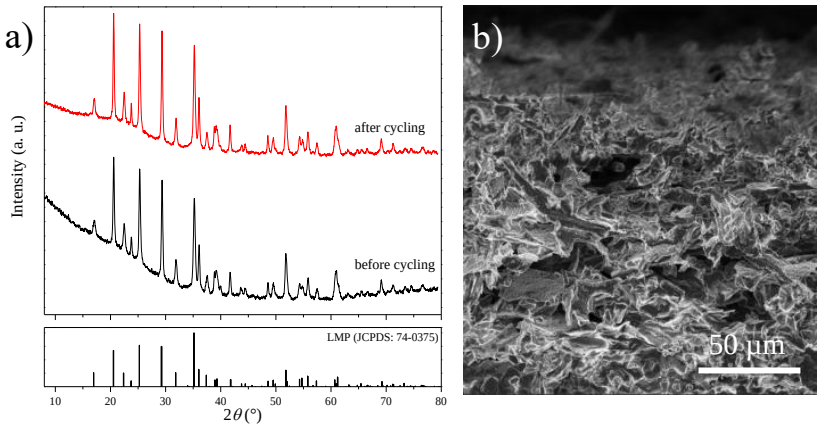


**Figure 6.** XRD patterns of freestanding LFMP/C/rGO electrode before and after the rate performance test (a). The bars at the bottom mark the position and the intensity of the diffraction lines of the olivine LMP structure (space group Pmnb, JCPDS no. 74-0375). SEM image of freestanding LFMP/C/rGO electrode after electrochemical testing (b).

For a convenient comparison of the data presented in this work with those reported in the literature, the rate performance and cycling stability measurements were also calculated for the mass of LFMP (active material) only, without considering the mass of the electrochemically inactive components (Figure 7 and S13a). Both the freestanding and the Al-foil-based LFMP/C/rGO electrodes demonstrate a reasonably good cycling stability. However, the freestanding composite reaches higher specific capacities. After 200 cycles at 2C, 122 mAh $g^{-1}_{LFMP}$ are obtained as compared to 80 mAh $g^{-1}_{LFMP}$ for the Al-foil-based composite (Figure S13b). The freestanding LFMP/C/rGO electrode also shows a superior rate performance (Figure 7 and S13a), as well as higher volumetric energy density (Figure S14). Additionally, the rate performance of freestanding electrodes having a higher mass loading was further investigated (Figure S15).

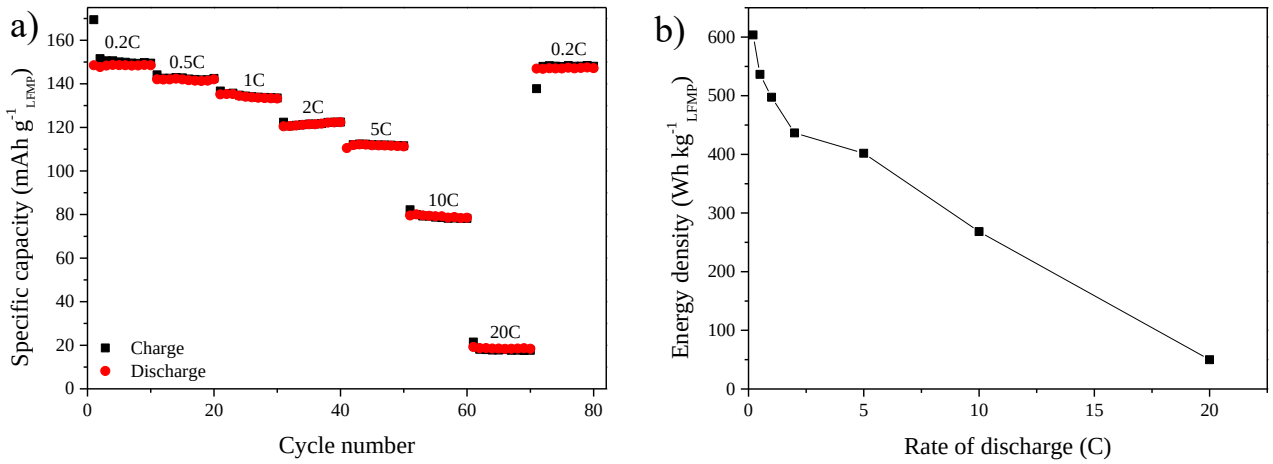


**Figure 7.** Rate performance (a) and the corresponding gravimetric energy density at different C-rates (b) of the freestanding LFMP/C/rGO nanocomposite (mass loading of 3 mg $cm^{-2}$).

The electrochemical performance of our freestanding LFMP/C/rGO nanocomposite is far superior to freestanding LFMP electrodes reported so far (Table S1). The freestanding electrospun $LiFe_{0.25}Mn_{0.75}PO_4$/C nanofiber composite reported by von Hagen et al. having a similar Mn to Fe ratio as our LFMP/C/rGO nanocomposite reaches around 60 mAh $g^{-1}_{LFMP}$ at 0.5C, as compared to 142 mAh $g^{-1}_{LFMP}$ for the freestanding LFMP/C/rGO nanocomposite reported in this work.[16] Additionally, the rate performance of our freestanding LFMP/C/rGO nanocomposite delivering 149, 142 and 134 mAh $g^{-1}_{LFMP}$ (Figure 7a) is also superior to 120, 112 and 110 mAh $g^{-1}_{LFMP}$ at 0.2C, 0.5C and 1C, respectively, reported for the best performing $LiFe_{0.5}Mn_{0.5}PO_4$/C nanofiber composite shown by von Hagen et al..[16]

The cycling and the rate performance of the freestanding LFMP/C/rGO nanocomposite can even keep up with those of freestanding LFP composites, calculated both for the active material loading or for the weight of the entire electrode (see Table S1 and S2), although LFP has a better electrical and ionic conductivity than LFMP. The LFP/graphene composite reported by Du et al. is one of the best performing freestanding LFP composites.[23] At 0.2C it retains a discharge capacity of 160 mAh $g^{-1}_{LFP}$, which is only slightly higher compared to our freestanding LFMP/C/rGO electrode. However, due to the higher working potential, the freestanding LFMP/C/rGO shows a significantly higher energy density of 604 Wh $kg^{-1}_{LFMP}$ (Figure 7b) as compared to 530 Wh $kg^{-1}_{LFP}$ (both at 0.2C) reported for the LFP composite material synthesized by Du et al. (the energy density was obtained by evaluation of the corresponding discharge curve).[23] This clearly illustrates that the freestanding LFMP/C/rGO nanocomposites are advantageous compared to freestanding LFP composites in terms of gravimetric capacity due to their increased working potential.

## CONCLUSION

Freestanding LFMP/rGO nanocomposites were fabricated via a novel simple freeze-casting route, involving ultrasonication of a suspension containing microwave–assisted synthesized LFMP nanoparticles, sucrose and GO, freeze drying and pyrolysis. The developed procedure enables fabrication of freestanding electrodes with a very high loading of active material of 83 wt%, high total loading of up to 8 mg $cm^{-2}$, high energy density, excellent cycling stability and at the same time very fast charging rate, with a total performance significantly exceeding the values reported in the literature. Discharge capacities of 103 mAh $g^{-1}_{electrode}$ and 122 mAh $g^{-1}_{LFMP}$ are obtained after 200 cycles at 2C, which corresponds to capacity retentions of 93% and 94%, respectively. The cycling stability is also much better as compared to LFMP/rGO coated on Al-foil. Under the same conditions a discharge capacity of only 80 mAh $g^{-1}_{LFMP}$ is retained. Moreover, the rate performance of the freestanding composite is also superior to Al-foil based equivalents, especially with regard to the entire weight of the electrode, as the freestanding electrode has a significantly lower amount of inactive material. This also translates to a high energy density of 604 Wh $kg^{-1}_{LFMP}$ for the freestanding composite which significantly outperforms that of LFP analogs. The keys to the improved performance of the freestanding LFMP/rGO electrodes are the use of GO with its high concentration of surface functional groups favoring the adhesion of high amounts of LFMP nanoparticles and, most importantly, the freeze-drying of the GO-based nanocomposites to prevent the morphology collapse and provide a unique fluffy structure of the freestanding electrodes. The important features of the developed procedure is its simplicity, as the LFMP nanoparticles with the optimum size are obtained in a easily scalable reaction in ethylene glycol; the nanocomposites with a homogeneous high loading of active material are achieved via a simple mixing of GO and LFMP nanoparticle suspensions, and a commercially established freeze drying process is used to obtained the optimized electrode morphology. Freestanding LFM/rGO nanocomposite electrodes with a high total energy and greatly reduced fraction of electrochemically inactive components offer an attractive alternative to conventional Al-foil based electrodes, and we envision that the developed procedure can be easily adapted to other active materials to obtain electrodes with even higher energy densities.

## EXPERIMENTAL SECTION

**Materials.** All chemicals were used as-received unless otherwise noted: Lithium hydroxide (LiOH, Sigma-Aldrich), ethylene glycol (EG, 99%, Sigma Aldrich), phosphoric acid ($H_3PO_4$; 99.999%, Sigma-Aldrich), manganese(II) sulfate monohydrate ($MnSO_4 \cdot H_2O$; 99%, Sigma Aldrich), iron(II) sulfate heptahydrate ($FeSO_4 \cdot 7H_2O$; 99%, Sigma Aldrich), L(+)-ascorbic acid ($C_6H_8O_6$, Riedel-de Haen), sucrose ($C_{12}H_{22}O_{11}$, Sigma-Aldrich), graphite microparticles (2–15 μm,

99.9995%, Alfa Aesar), poly(vinylidene fluoride) (PVDF, Sigma-Aldrich), carbon black (Super C65, Timcal), 1-methyl-2-pyrrolidone (NMP, Sigma-Aldrich), PuriEL electrolyte (1.15 M $LiPF_6$ in EC/EMC/DMC = 2:2:6 v/v + 1.0 %wt FEC, soulbrain MI), lithium metal (Rockwood) and aluminum foil (Targray). Sulphuric acid (98%), phosphoric acid (85%), potassium permanganate (99.5%), hydrogen peroxide (30%), barium nitrate (99.5%) and *N*,*N*-dimethylformamide (DMF) were obtained from Penta, Czech Republic.

**Synthesis of LFMP nanoparticles.** LFMP nanoparticles were synthesized in a solvothermal microwave-assisted route. In a first step 144 mg (6 mmol) LiOH was dissolved in 8 mL EG at 50 °C. After stirring for 1 h a solution of 196 mg (2 mmol) $H_3PO_4$ in 4 mL EG was added dropwise and the resulting white suspension was stirred for 0.5 h. 111 mg (0.4 mmol) $FeSO_4$, 270 mg (1.6 mmol) $MnSO_4$ and 35 mg (0.2 mmol) ascorbic acid were dissolved in 1 mL water. This solution was subsequently added to the $LiOH/H_3PO_4$/EG dispersion. The resulting slightly yellow suspension was in turn stirred for 0.5 h at room temperature, transferred to a Teflon-lined microwave autoclave and heated to 170 °C under microwave irradiation (Synthos 3000, Anton Paar; initial heating power 800 W) for 25 min. The resulting ochre suspension was washed several times by repeated centrifugation (22500 rcf for 15 min) and redispersion in deionized water and ethanol, respectively, and finally dried at 60 °C overnight.

**Synthesis of graphene oxide suspension.** A graphene oxide suspension was prepared with slight modification as described by Marcano et al..[45] In brief, 3.0 g graphite and 18.0 mg potassium permanganate were subsequently added to a cooled (below 0 °C) mixture of concentrated sulfuric acid (360 mL) and phosphoric acid (40 mL). The mixture was heated at 50 °C for 12 h under stirring. Afterwards, the mixture was cooled to room temperature and then poured on ice. Afterwards, a 30 % Hydrogen peroxide (3.0 mL) solution was added. After the ice was molten, hydrogen peroxide (30 mL) and water (2500 mL) were added. The obtained graphene oxide was washed by repeated centrifugation and redispersion in deionized water until a negative reaction on sulfate ions with $Ba(NO_3)_2$ was achieved. The graphene oxide slurry was ultrasonicated for 1 h to exfoliate the GO sheets. The concentration of GO in this suspension was measured to be 20.4 mg $mL^{-1}$ by gravimetric analysis.

**Fabrication of LFMP/C/rGO freestanding nanocomposites.** 130 mg of LFMP nanoparticles were mixed with 43 mg sucrose, 1.8 mL GO suspension and 40 mL water. The brown suspension was ultrasonicated for 2.5 h and then poured on aluminum blocks which were cooled with liquid nitrogen in advance. The LFMP/GO composite was removed and freeze dried for two days. The nanocomposite was finally pyrolyzed in nitrogen at 350 °C for 4 h followed by 650 °C for 4 h; each heating step was reached with a ramp of 5 °C $min^{-1}$.

**Battery assembly.** The electrochemical measurements were conducted on ECC-PAT-Core electrochemical test cells (EL-Cell). LFMP/C/rGO freestanding composites were cut into size (discs with a diameter of 18 mm) and used directly as working electrodes, without the addition of extra carbon black or PVDF. The freestanding LFMP/C/rGO electrodes had an LFMP mass loading of 3 to 3.5 mg $cm^{-2}$ and for the high loading composite a mass loading of 8 mg $cm^{-2}$. For reference experiments “conventional electrodes” were prepared as well. For that purpose, LFMP/C/rGO was mixed with PVDF and carbon black at a mass ratio of 80:10:10 in NMP. The slurry was stirred for one day and then uniformly coated onto Al foil using the doctor blade technique (wet film thickness 100 µm, equaling to a LFMP mass loading of 0.6 mg $cm^{-2}$). The electrodes were dried at 60 °C for 8 h and afterwards in vacuum at 120 °C for 4 h before being used as cathodes. The cells were assembled in an argon filled glove box (Labstar 1250/750, MBraun, Germany) with lithium metal foil as counter and reference electrode, glass fiber membrane (El-CELL ECC1-01-0011-A/L) as separator and a commercial electrolyte consisting of 1.15 M $LiPF_6$ in EC/EMC/DMC at a 2:2:6 volume ratio and 1.0 %wt FEC.

**Characterization methods.** Wide angle X-ray diffraction was performed in transmission mode using a STOE STADI P diffractometer with Cu Kα1-radiation (λ = 1.54060 Å) and a Ge(111) single crystal monochromator equipped with a DECTRIS solid state strip detector MYTHEN 1K. Powder XRD patterns were measured in a $2\theta$ range from 5° to 70° with a step size of 1° and a fixed counting time of 90 s per step.

ICP-OES analysis was performed on a VARIAN VISTA RL OCD.

Raman spectra were collected at room temperature in a backscattering configuration using an inVia Raman microscope (RENISHAW), equipped with a charge-coupled device detector and a 532 nm He-Ne laser.

FTIR measurements were performed on an iS50R FTIR spectrometer (Thermo Scientific, USA) in ATR configuration using a KBr beamsplitter in the range of 4000–400 $cm^{-1}$ at a resolution of 4 $cm^{-1}$.

Combustion elemental analysis (CHNS-O) was carried out on a PE 2400 Series II CHNS/O Analyzer (Perkin Elmer, USA). The instrument was used in a CHN operating mode.

TGA measurements were carried out on a NETZSCH STA 440 C TG/DSC machine at a heating rate of 10 °C $min^{-1}$ in a stream of synthetic air of about 25 mL $min^{-1}$.

Nitrogen sorption measurements were carried out at 77 K using a QUANTACHROME Nova Station C. Before the sorption experiments, the samples were degassed under vacuum for 12 h at 120 °C. The specific surface area was determined by the BET method in the range of $p/p° = 0.05–0.2$. Density functional theory (DFT)/Monte Carlo methods and a nonlocal density functional theory adsorption model with cylindrical pores was used to calculate the pore size distribution.

SEM images were acquired with an FEI Helios NanoLab G3 UC scanning electron microscope having a field emission gun operated at 3-5 kV. EDX analysis was conducted at an operating voltage of 20 kV using an X $Max^N$ Silicon Drift Detector with 80 $mm^2$ detector area (OXFORD INSTRUMENTS) and AZTec acquisition software (OXFORD INSTRUMENTS). The samples were suspended in ethanol and drop-coated on a silicon wafer which was then glued onto a sample holder with silver lacquer. The freestanding composites were also measured on carbon tabs glued onto a sample holder

S/TEM measurements were performed on an FEI Titan Themis equipped with a field emission gun operated at 120 or 300 kV, a high-angle annular dark-field (HAADF) detector and a Super-X energy-dispersive X-ray spectrometer. The samples were dispersed in ethanol and drop-coated on a copper grid with a holey carbon film.

XPS measurements were carried out on an X-ray photoelectron Phoibos 100 MCD-5 spectrometer (SPECS, Germany) using an Al X-ray radiation source (1486.7 eV). The samples were placed on a carbon black tape. The measured values were referenced to an adventitious carbon peak at 285 eV.

Conductivity measurements were performed on an ECOPIA HMS 3000 system in Van der Pauw geometry.

Electrochemical measurements were carried out at 20 °C with ECC-PAT-Core (EL-Cell) battery test cells using an Autolab potentiostat/galvanostat (PGSTAT302N) with a FRA32M module or an Autolab Multipotentiostat M101 equipped with an 8AUT.M101 module operated with Nova 1.11 software. Cyclic voltammetry was conducted in a potential range of 2.0-4.5 V vs. $Li/Li^+$ at scan rates of 0.1, 0.2, 0.5, 1, 1.5 and 2.0 mV $s^{-1}$. Galvanostatic charge/discharge

measurements were carried out at different C rates (0.2-20C) in a voltage window of 2.0-4.5 V. Electrochemical impedance spectroscopy was performed between 100-0.001 kHz with an applied sinusoidal amplitude of 10 mV.

## AUTHOR INFORMATION


### Corresponding Author

*E-mail: d.fattakhova@fz-juelich.de


## ACKNOWLEDGMENTS


The authors are grateful for funding from the German Research Foundation (DFG, grant nos. FA 839/3-1 and SPP 1613), to the *e*-conversion and NIM Excellence Clusters (DFG), and to the Center for NanoScience (CeNS) as well as the German Federal Ministry of Education and Research (BMBF, Project CatSe). Z.S. and J.L. were supported by Czech Science Foundation (GACR No. 20-16124J). The authors acknowledge Tina Reuther for sorption and TGA measurements.


## APPENDIX A. SUPPLEMENTARY DATA

Supplementary data to this article can be found online at…

## REFERENCES


(1) H. Zhuang, Y. Bao, Y. Nie, Y. Qian, Y. Deng, G. Chen, Synergistic effect of composite carbon source and simple pre-calcining process on significantly enhanced electrochemical performance of porous $LiFe_{0.5}Mn_{0.5}PO_4$/C agglomerations. *Electrochim Acta* 2019, *314*, 102-114.

(2) Y. Deng, C. Yang, K. Zou, X. Qin, Z. Zhao, G. Chen, Recent Advances of Mn-Rich $LiFe_{1-y}MnyPO_4$ ($0.5 \leq y < 1.0$) Cathode Materials for High Energy Density Lithium Ion Batteries. *Adv. Energy Mater.* **2017**, *7*, 1601958.

(3) M. Zhang, N. Garcia-Araez, A. L. Hector, Understanding and development of olivine $LiCoPO_4$ cathode materials for lithium-ion batteries *J. Mater. Chem. A* **2018**, *6*, 14483-14517.

(4) T. Ruan, B. Wang, F. Wang, R. Song, F. Jin, Y. Zhou, D. Wang, S. Dou, Stabilizing the structure of $LiMn_{0.5}Fe_{0.5}PO_4$via the formation of concentration-gradient hollow spheres with Fe-rich surfaces. *Nanoscale* **2019**, *11*, 3933-3944.

(5) J. Ludwig, T. Nilges, Recent progress and developments in lithium cobalt phosphate chemistry- Syntheses, polymorphism and properties. *J. Power Sources* **2018**, *382*, 101-115.

(6) V. Aravindan, J. Gnanaraj, Y. S. Lee, S. Madhavi, LiMnPO4 – A next generation cathode material for lithium-ion batteries. *J. Mater. Chem. A* **2013**, *1*, 3518-3539.

(7) R. A. Susantyoko, T. S. Alkindi, A. B. Kanagaraj, B. An, H. Alshibli, D. Choi, S. AlDahmani, H. Fadaq, S. Almheiri, Performance optimization of freestanding MWCNT-$LiFePO_4$ sheets as cathodes for improved specific capacity of lithium-ion batteries. *RSC Adv.* **2018**, *8*, 16566-16573.

(8) Z. Deng, Q. Wang, D. Peng, H. Liu, Y. Chen, Fast precipitation-induced $LiFe_{0.5}Mn_{0.5}PO_4$/C nanorods with a fine size and large exposure of the (010) faces for high-performance lithium-ion batteries. *J. Alloys Compd.* **2019**, *794*, 178-185.

(9) J. Li, Y. Wang, J. Wu, H. Zhao, H. Liu, CNT-embedded $LiMn_{0.8}Fe_{0.2}PO_4$/C microsphere cathode with high rate capability and cycling stability for lithium ion batteries. *J. Alloys Compd.* **2018**, *731*, 864-872.

(10) D. Wang, H. Buqa, M. Crouzet, G. Deghenghi, T. Drezen, I. Exnar, N. H. Kwon, J.H. Miners, L. Poletto, M. Grätzel, High-performance, nano-structured $LiMnPO_4$ synthesized via a polyol method. *J. Power Sources* **2009**, *189*, 624-628.

(11) L. Yang, Y. Wang, J. Wu, M. Xiang, J. Li, B. Wang, Y. Zhang, H. Wu, H. Liu, Facile synthesis of micro-spherical $LiMn_{0.7}Fe_{0.3}PO_4$/C cathodes with advanced cycle life and rate performance for lithium-ion battery. *Ceram. Inter.* **2017**, **43**, 4821-4830.

(12) J. N. Zhu, W. C. Li, F. Cheng, A. H. Lu, Synthesis of $LiMnPO_4$/C with superior performance as Li-ion battery cathodes by a two-stage microwave solvothermal process. *J. Mater. Chem. A* **2015**, *3*, 13920-13925.

(13) M. Jo, H. Yoo, Y. S. Jung, J. Cho, Carbon-coated nanoclustered $LiMn_{0.71}Fe_{0.29}PO_4$ cathode for lithium-ion batteries. *J. Power Sources* **2012**, *216*, 162-168.

(14) Z. Lei, A. Naveed, J. Lei, J. Wang, J. Yang, Y. Nuli, X. Meng, Y. Zhao, High performance nano-sized $LiMn_{1-x}Fe_xPO_4$ cathode materials for advanced lithium-ion batteries. *RSC Adv.* **2017**, *7*, 43708-43715.

(15) K. Kretschmer, B. Sun, X. Xie, S. Chen, G. Wang, A free-standing $LiFePO_4$–carbon paper hybrid cathode for flexible lithium-ion batteries. *Green Chem.* **2016**, *18*, 2691-2698.

(16) R. von Hagen, H. Lorrmann, K. C. Möller, S. Mathur, Electrospun $LiFe_{1-y}Mn_yPO_4$/C Nanofiber Composites as Self-Supporting Cathodes in Li-Ion Batteries. *Adv. Energy Mater.* **2012**, *2*, 553-559.

(17) R. A. Susantyoko, Z. Karam, S. Alkhoori, I. Mustafa, C. H. Wu, S. A. Almheiri, Surface-engineered tape-casting fabrication technique toward the commercialisation of freestanding carbon nanotube sheets. *J. Mater. Chem. A* **2017**, *5*, 19255-19266.

(18) C. Zhang, L. Yao, Y. Qiu, Synthesis and characterization of $LiFePO_4$–carbon nanofiber–carbon nanotube composites prepared by electrospinning and thermal treatment as a cathode material for lithium-ion batteries. *J. Appl. Polym. Sci.* **2016**, *133*, 43001.

(19) A. B. Kanagaraj, P. Chaturvedi, B. H. An, S. AlDahmani, H. Fadaq, D. S. Choi, Electrochemical performance of freestanding $LiFePO_4$/MWCNT composite electrodes and its ex situ studies. Ionics **2019**, DOI: 10.1007/s11581-019-03168-1.

(20) H. Xiao, J. P. Pender, M. A. Meece-Rayle, J. P. de Souza, K. C. Klavetter, H. Ha, J. Lin, A. Heller, C. J. Ellison, C .B. Mullins, Reduced-Graphene Oxide/Poly(acrylic acid) Aerogels as a Three-Dimensional Replacement for Metal-Foil Current Collectors in Lithium-Ion Batteries. *ACS Appl. Mater. Interfaces* **2017**, *9*, 22641-22651.

(21) N. Li, Z. Chen, W. Ren, F. Li, H. M. Cheng, Flexible graphene-based lithium ion batteries with ultrafast charge and discharge rates. *Proc. Natl. Acad. Sci.* **2012**, *109*, 17360.

(22) Y. H. Ding, H. M. Ren, Y. Y. Huang, F. H. Chang, P. Zhang, Three-dimensional graphene/$LiFePO_4$ nanostructures as cathode materials for flexible lithium-ion batteries. *Mater. Res. Bull.* **2013**, *48*, 3713-3716.

(23) Y. Du, Y. Tang, F. Huang, C. Chang, Preparation of three-dimensional free-standing nano-$LiFePO_4$/graphene composite for high performance lithium ion battery. *RSC Adv.* **2016**, *6*, 52279-52283.

(24) B. Wang, Y. Xie, T. Liu, H. Luo, B. Wang, C. Wang, L. Wang, D. Wang, S. Dou, Y. Zhou, $LiFePO_4$ quantum-dots composite synthesized by a general microreactor strategy for ultra-high-rate lithium ion batteries. *Nano Energy* **2017**, 42, 363-372.

(25) J. J. Bao, B. K. Zou, Q. Cheng, Y. P. Huang, F. Wu, G. W. Xu, C. H. Chen, Flexible and free-standing $LiFePO_4$/TPU/SP cathode membrane prepared via phase separation process for lithium ion batteries. *J. Membr. Sci.* **2017**, *541*, 633-640.

(26) L. Jabbour, M. Destro, D. Chaussy, C. Gerbaldi, N. Penazzi, S. Bodoardo, D. Beneventi, Flexible cellulose/$LiFePO_4$ paper-cathodes: toward eco-friendly all-paper Li-ion batteries. *Cellulose* **2013**, *20*, 571-582.

(27) Y. Wang, Z. Y. He, Y. X. Wang, C. Fan, C. R. L. Liu, Q. L. Peng, J. J. Chen, Z. S. Feng, Preparation and characterization of flexible lithium iron phosphate/graphene/cellulose electrode for lithium ion batteries. *J. Colloid Interface Sci.* **2018**, *512*, 398-403.

(28) B. S. Lalia, T. Shah, R. Hashaikeh, Microbundles of carbon nanostructures as binder free highly conductive matrix for $LiFePO_4$ battery cathode. *J. Power Sources* **2015**, *278*, 314-319.

(29) L. Mahmoud, B. S. Lalia, R. Hashaikeh, Carbon nanostructures modified $LiFePO_4$ cathodes for lithium ion battery applications: optimized porosity and composition. *Mater. Res. Express* **2016**, *3*, 125008.
(30) H. Li, L. Peng, D. Wu, J. Wu, Y. J. Zhu, X. Hu, Ultrahigh-Capacity and Fire-Resistant $LiFePO_4$-Based Composite Cathodes for Advanced Lithium-Ion Batteries. *Adv. Energy Mater* **2019**, *9*, 1802930.
(31) L. L. Chen, X. Q. Shen, M. X. Jing, S. W. Zhu, Z. C. Pi, J. Q. Li, H. A. Zhai, K. S. Xiao, Electrospun $LiFePO_4$/C composite fiber membrane as a binder-free, self-standing cathode for power lithium-ion battery *J. Nanosci. Nanotechnol.* **2018**, *18*, 4720-4727.
(32) O. Toprakci, H. A. K. Toprakci, L. Ji, G. Xu, Z. Lin, X. Zhang, Carbon Nanotube-Loaded Electrospun $LiFePO_4$/Carbon Composite Nanofibers As Stable and Binder-Free Cathodes for Rechargeable Lithium-Ion Batteries. *ACS Appl. Mater. Interfaces* **2012**, *4*, 1273-1280.
(33) D. Ding, Y. Maeyoshi, M. Kubota, J. Wakasugi, K. Kanamura, H. Abe, A Facile Way To Synthesize Carbon-Coated $LiMn_{0.7}Fe_{0.3}PO_4$/Reduced Graphene Oxide Sandwich-Structured Composite for Lithium-Ion Batteries. *ACS Appl. Energy Mater* **2019**, *2*, 1727-1733.
(34) X. Yan, D. Sun, Y. Wang, Z. Zhang, W. Yan, J. Jiang, F. Ma, J. Liu, Y. Jin, K. Kanamura, Enhanced Electrochemical Performance of $LiMn_{0.75}Fe_{0.25}PO_4$ Nanoplates from Multiple Interface Modification by Using Fluorine-Doped Carbon Coating. *ACS Sustain. Chem. Eng.* **2017**, *5*, 4637-4644.
(35) Z. Dai, L. Wang, X. He, F. Ye, C. Huang, J. Li, J. Gao, J. Wang, G. Tian, M. Ouyang, Morphology regulation of nano $LiMn_{0.9}Fe_{0.1}PO_4$ by solvothermal synthesis for lithium ion batteries. *Electrochim. Acta* **2013**, *112*, 144-148.
(36) S. Kabiri, D. N. H. Tran, M. A. Cole, D. Losic, Functionalized three-dimensional (3D) graphene composite for high efficiency removal of mercury. *Sci. Water Res. Technol.* **2016**, *2*, 390-402.
(37) L. Yang, X. Jiang, Z. S. Yang, W. J. Jiang, Effect of $MnSO_4$ on the Removal of $SO_2$ by Manganese-Modified Activated Coke. *Ind. Eng. Chem. Res.* **2015**, *54*, 1689-1696.
(38) X. Huang, X. He, C. Jiang, G. Tian, Morphology evolution and impurity analysis of $LiFePO_4$ nanoparticles via a solvothermal synthesis process. *RSC Adv.* **2014**, *4*, 56074-56083.
(39) J. Ludwig, D. Haering, M. M. Doeff, T. Nilges, Particle size-controllable microwave-assisted solvothermal synthesis of the high-voltage cathode material LiCoPO4 using water/ethylene glycol solvent blends. *Solid State Sci.* **2017**, *65*, 100-109.
(40) K. Okada, I. Kimura, K. Machida, High rate capability by sulfur-doping into $LiFePO_4$ matrix. *RSC Adv.* **2018**, *8*, 5848-5853.
(41) L. Guo, L. Ren, L. Wan, J. Li, Heterogeneous carbon/N-doped reduced graphene oxide wrapping $LiMn_{0.8}Fe_{0.2}PO_4$ composite for higher performance of lithium ion batteries. *Appl. Surf. Sci.* **2019**, *476*, 513-520.
(42) L. An, Z. Li, X. Ren, L. Wang, G. Liang, Low-cost synthesis of $LiMn_{0.7}Fe_{0.3}PO_4$/C cathode materials with $Fe_2O_3$ and $Mn_3O_4$ via two-step solid-state reaction for lithium-ion battery. *Ionics* **2019**, *25*, 2997-3007.
(43) J. Li, Y. Wang, J. Wu, H. Zhao, H. Wu, Y. Zhang, H. Liu, Preparation of Enhanced-Performance $LiMn_{0.6}Fe_{0.4}PO_4$/C Cathode Material for Lithium-Ion Batteries by using a Divalent Transition-Metal Phosphate as an Intermediate. *ChemElectroChem* 2016, *4*, 175-182.
(44) F. Zoller, K. Peters, P. Zehetmaier, P. Zeller, M. Döblinger, T. Bein, Z. Sofer, D. Fattakhova-Rohlfing, Making ultrafast high capacity anodes for lithium batteries via antimony doping of nanosized tin oxide/graphene composites. *Adv. Funct. Mater.* 2018, *28*, 1706529.
(45) D. C. Marcano, D. V. Kosynkin, J. M. Berlin, A. Sinitskii, Z. Sun, A. Slesarev, L. B. Alemany, W. Lu, J. M. Tour, Improved Synthesis of Graphene Oxide. *ACS Nano* **2010**, *4*, 4806-4814.